The International Journal of Advanced Manufacturing Technology (2024) 134:811–823
https://doi.org/10.1007/s00170-024-14150-1

ORIGINAL ARTICLE

Experimental and simulative investigations of burr formation in planing of AISI 1045

Gero Polus[1] · Jannis Saelzer[1] · Sven Brock[2] · Heiko Pleskun[2] · Dirk Biermann[1] · Andreas Brümmer[2]

Received: 12 February 2024 / Accepted: 15 July 2024 / Published online: 27 July 2024

Abstract
The clearance flow in dry-running vacuum pumps is the main loss mechanism. To reduce the clearance mass flow rate in rarefied gas flows, sawtooth structures transversing to the direction of flow can be utilized. However, due to the sawtooth's structure size, micro-machining is necessary, whereby burr formation is a central challenge. First, the effectiveness of non-idealized sawtooth structures is investigated, demonstrating a high sensibility of the performance regarding the geometry of the tip. Therefore, burr formation in the cutting process must be minimized. For this reason, a 3D finite element (FE) chip formation model capable of predicting the burr formation is developed. An analysis of the burr formation zone showed positive triaxialities; thus, the triaxiality-dependent Johnson–Cook damage model is utilized. To minimize the mesh-induced error, a convergence analysis is conducted, showing no convergence of the maximum burr height. This is caused by the pathological mesh size dependence of local continuum damage models. A comparison of the cutting experiments and simulations revealed a reasonable prediction of cutting forces. In contrast, the passive force is predicted poorly, which is attributed to the underestimation of the ploughing force for non-elastic simulations. The prediction quality regarding the maximum burr height differs for the investigated cutting speeds, which can be explained by a built-up edge and a change in the machine tool compliance. Thereby, an analysis of the burr formation revealed that the burr height is captured by a non-physical remeshing algorithm and that the burr volume might be a more appropriate characteristic.

Keywords FEM · Cutting · Burr formation · AISI 1045 · Rarefied gap flow

1 Introduction

The vacuum technology is an essential part for many industry-relevant processes, e.g. physical and chemical vapour deposition. Therefore, the development of dry-running vacuum pumps is a current focus of the research community [1]. For these pumps, the clearance flow between the moving parts and the housing is the main loss mechanism. Sazhin [2] demonstrated that in case of a rarefied gas flow through a gap of two flat surfaces, the mass flow rate can be significantly reduced by introducing a sawtooth structure transverse to the direction of flow. Thereby, a low ratio ($< 10^{-1}$) of the sawtooth structure height to the clearance value is important for optimal performance. This technology is a promising approach to reduce the clearance flow in dry running vacuum pumps. However, typical clearance values are in the range of $l_{cl} = 0.3 \ldots 0.05$ mm [3]; thus, the sawtooth structures can only be manufactured by means of micro-machining. In general, different machining procedures can be used for micro-machining, e.g. fly-cutting, turning and grinding [4]. Another procedure is micro-milling, which is capable of manufacturing complex 3D parts [5]. However, to produce accurate sawtooth structures in flat surfaces, planing is suitable [6]. A central challenge in micro-machining is burr formation because the dimensions of the burrs can have the same magnitude as the structure itself.

The following work is structured as follows. First, the performance of non-idealized sawtooth structures in rarefied flows is investigated. These novel findings give important insights regarding the shape accuracy requirements of the surface structure and thus represent an additional motivation of the following investigations regarding burr formation. Then, a comprehensive state of the art concerning burr

✉ Gero Polus
gero.polus@tu-dortmund.de

[1] Institute of Machining Technology, TU Dortmund University, 44227 Dortmund, Germany

[2] Chair of Fluidics, TU Dortmund University, 44227 Dortmund, Germany

formation is presented before friction, and cutting experiments are being conducted. In the cutting experiments, a cutting strategy with a constant uncut chip thickness was considered, to focus on the fundamental mechanisms of burr formation. Afterwards, a 3D FE simulation capable of predicting the maximum burr height is developed, whereby the results from the friction experiments are an important input parameter. Lastly, a validation of the FE model using data obtained from cutting experiments is performed.

2 Performance of non-idealized sawtooth structures

Fluid flows result from the chaotic movements of particles interacting with each other and the surrounding walls. In rarefied flows, these particle movements themselves must be considered and, moreover, intermolecular interactions are comparatively rare, so that the flow is significantly influenced by wall interactions. These collisions can be modelled by the diffuse reflexion, whereby the particles are scattered on average normal to the wall. Therefore, surface structures can be used deliberately to influence the rarefied flow. Sazhin investigated this behaviour for pressure-driven flows through a gap of two flat surfaces using ideal sawtooth profiles, which can reduce the mass flow by up to 25% [2, 7]. However, due to the limited sharpness of geometrically defined cutting edges, an ideal sawtooth structure cannot be manufactured. For this reason, this section investigates the influence of tip and root rounding of a sawtooth structure and its influence to manipulate the reflection properties of molecules in rarefied gas flows. For this, a free molecular shear-driven air flow between two parallel walls is considered, neglecting intermolecular collisions. One wall is moving in flow direction with $c_w = 30$ m/s, and the other wall is static (see Fig. 12). The temperature is considered to be $T = 20$ °C. If both walls are technically smooth and diffuse wall scattering is applied, the resulting mass flow rate can be calculated by

$$\dot{m}_{\text{smooth}} = 0.5\rho l_{cl} w_{cl} c_w \tag{1}$$

incorporating the density ρ and the smallest cross section area $A = l_{cl} w_{cl}$ [8].

Now, the mass flow rate for such a channel is simulated using the Monte Carlo method. The static wall has a periodic surface structure transverse to the direction of flow. Therefore, a large number of molecules are simulated that are scattered from the moving wall back to the static wall, whereby they receive a new velocity vector based on diffuse wall scattering. The resulting mass flow rate is

$$\dot{m} = \rho l_{cl} w_{cl} \bar{c} \tag{2}$$

and the mean velocity $\bar{c}$ can be calculated as a weighted average of the velocities of all simulated molecules [7].

The different microstructures for the static wall investigated in this study are sketched in Fig. 1. The dashed reference profile is a sawtooth profile with symmetric opening

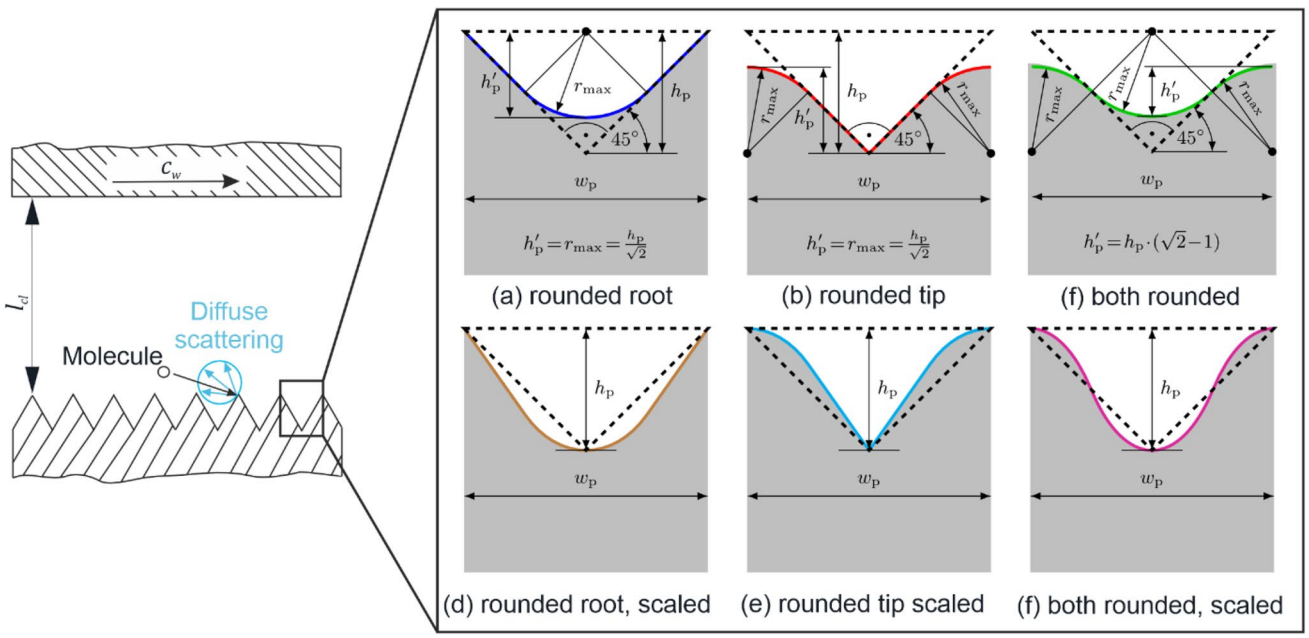

Fig. 1 Different profiles derived from the ideal sawtooth structure by rounding root and/or tip and optional scaling. Here, the maximum radius is shown

angle $\varphi = 90°$. This profile is modified by rounding the tip and/or root with different radii r, where the maximum radius r_{max} is defined such that the curvatures of tip and root do not overlap. As the resulting profiles vary in structure height h_p' (Fig. 1a–c), they are additionally scaled to ensure a constant profile width w_p and height h_p (Fig. 1d–f). For a free molecular flow, the overall size of the structure does not influence the results, as long as $h_p \ll l_{cl}$, and thus, only the periodic shape is important.

Figure 2 shows the ratio of the resulting mass flow rate for the different microstructure shapes related to the technically smooth walls for equal boundary conditions and channel height. A normalized mass flow rate of one would refer to smooth walls and a smaller value shows the reduction due to the surface structure. A normalized radius $r^* = r/r_{max} = 0$ refers to the ideal sawtooth profile. It is obtained that the sawtooth profile with a symmetric opening angle $\varphi = 90°$ reduces the resulting mass flow rate to about 68% compared to the flow between two smooth walls. For the unscaled profiles, the worst performance can be observed when both root and tip are rounded, leading to a linearly dependent mass flow rate with respect to the normalized radius r^*. However, even the worst profile investigated provides a reduction of 20% compared to smooth walls. Regarding the green and the blue curve, it is shown that the main effect is related to a curvature at the tip (red curve), while a curvature on the root only slightly affects the integral mass flow rate. The scaled profiles perform better than their corresponding counter parts, which can be related to a smaller effective opening angle. Especially for a rounded and scaled root structure, a reduction of the mass flow rate compared to the ideal sawtooth structure is observed. Further investigations to optimize the profile geometry are on-going.

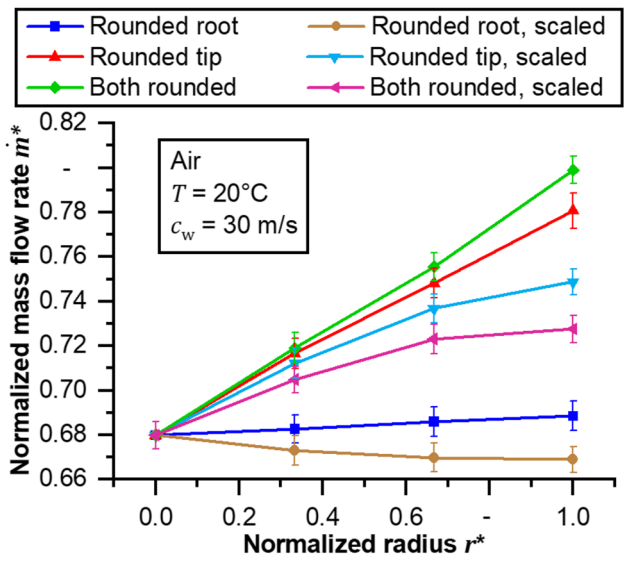

Fig. 2 Normalized mass flow rate against normalized radius with rounded root and/or tip with/without scaling. Error bars represent $\pm 3\sigma$ confidence interval

These investigations give important insights regarding the shape accuracy requirements of the surface structure for rarefied flows. Deviations from the ideal root geometry do not influence the normalized mass flow rate significantly, which is an important consideration for future tool development. Furthermore, the performance of this method is sensitive to the geometry of the tip; thus, burr formation must be minimized.

3 State of the art of burr formation

In machining, a distinction is made between three basic process variants: orthogonal (free), oblique (free) and oblique non-free cutting [9]. These process variants are defined for different manufacturing processes, e.g. turning and planing. Due to the favourable experimental conditions (e.g. stationary tool, good accessibility), the latter is suitable for experimental investigations. It allows conclusions to be drawn about more widespread manufacturing processes such as turning via the analogy of the basic process variants. For this reason, the planing process has already been studied in detail, whereby it has mostly been referred as one of the basic process variants. Consequently, the following state of the art focuses on these.

In micro-machining, burr formation is a central challenge. Gillespie and Blotter [10] identified four basic types of machining burrs based on their formation mechanism: Poisson burr, rollover burr, tear burr and cut-off burr. Nakayama and Arai [11] introduced a two-system classification for burr characterization. System 1 focuses on the cutting edge which is concerned with burr formation (major or minor cutting edge), while system 2 describes the direction of burr formation, e.g. backward and sideward. Furthermore, they were able to observe a decrease in burr height for a lower shear strain in the chip formation process. A reduction in shear strain can for example be attained due to high rake angles, high cutting speeds and the use of lubrication. Beier and Nothnagel [12] described a model for burr formation in metal cutting. According to this model, a penetration of the cutting tool into the workpiece causes a 3D stress cone. Once the elastic deformation capability of the workpiece is exceeded, plastic deformation occurs. Thereby, the material flow occurs in the direction of least resistance, if possible, into the direction of no material. This can cause a burr at the border of the tool trajectory.

Pekelharing [13] introduced a model for a negative shear plane on exit burr formation in orthogonal cutting. This model was used by Ko and Dornfeld [14] to develop an analytical model of exit burr formation for ductile metals. Chern and Dornfeld [15] defined three stages of burr formation in

orthogonal cutting: initiation, burr development and final burr formation. Later, Chern [16] differentiated between burr formation and edge breakout. The former is caused by bending and shearing along the negative deformation zone leading to a shear rupture, whereas the latter is the result of crack propagation, leading to either shear or normal rupture. Zannoun and Schoop [17] analysed exit burr formation for Inconel 718 via digital image correlation and showed that tool wear is also an important consideration. Min et al. [18] also studied exit burr formation in orthogonal cutting, using a 2D FE model. Based on this, an analytical model for burr formation in drilling was developed. Finally, a 3D FE model was introduced which is capable of predicting uniform and crown burrs. Thereby, the thickness of the plastic region at the exit surface is essential. For a thin layer, the support of the material is insufficient and very little cutting at the perimeter of the drill occurs, resulting in a uniform burr. However, for a thicker layer, the material at the perimeter of the drill can be cut, causing fracture at the drill tip and resulting in a crown burr. Asad et al. [19] used FE simulations to study exit burr length in orthogonal cutting of AA2024. The authors' analysis showed an increase in burr length with a reduction in rake angle and an increase in feed. Zou et al. [20] studied the influence of a backup material on exit burr in orthogonal cutting. The authors showed that using backup material can be an effective option in reducing burr size. Further, authors analysed exit burr formation in oblique cutting, e.g. [21] and [22]. Li et al. [23] employed the Boussinesq-Flamant problem, in order to predict the side burr size in oblique non-free cutting at the major and minor cutting edges while using backup material. The authors compared their predicted values with experimental and simulative data and showed a good accuracy. Deng et al. [24] and Pang et al. [25] studied side burr formation at the minor cutting edge in oblique non-free cutting of Al6061 and copper, respectively. The authors investigated the influence of rake angle, feed rate and cutting speed. They concluded that the side burr height increases significantly for lower rake angles and higher feed rates, while it did decrease slightly with an increase in cutting speed.

In summary, the formation of exit burrs in metal cutting has been studied in detail. However, the formation of side burrs, especially focusing on steels, is yet not investigated very well. For this reason, side burr formation at the minor cutting edge in planing (oblique non-free cutting) of AISI 1045 is studied in this work.

4 Experimental boundary conditions

Within the scope of this work, friction and cutting experiments were conducted. For both, a special machine tool of the company *Heinz Berger Maschinenfabrik GmbH & Co. KG* was utilized. This machine is able to accelerate with a= 30 m/s^2 to a relative speed of v_{rel} = 180 m/min.

For the characterization of the friction behaviour between the workpiece and the tool, a testing rig based on Puls et al. has been adopted [26]. Thereby, the relative speed is varied between v_{rel} = 16 … 180 m/min. A detailed description of the experimental set-up can be found in [27].

Figure 3 shows the experimental setup for the cutting experiments. The workpiece made of AISI 1045 with a tensile strength of 685 MPa and a hardness of 192 HV10 has a length of l_{wp} = 140 mm and was prepared with a multitude of 2-mm-wide longitudinal bars. The tool material was cemented carbide HF K40 consisting of 90% tungsten and 10% cobalt. The geometry of the tool is described by a flank angle, rake angle and cutting edge radius of $\alpha = 10°$, $\gamma = 0°$ and $r_\beta = 20$ µm, respectively. In order to measure the mechanical loads during the experiments, the tool holder was clamped into the dynamometer *Kistler 9263*. Utilizing the piezoelectric effect, it can be used to measure forces up to ± 10 kN in the x- and y-direction and ± 20 kN in the z-direction. Furthermore, the high-speed camera *Keyence VW-600M* was used to get a detailed view of the burr formation process. The planing process was conducted as an oblique non-free cut with a width of cut of b = 1.5 mm and an uncut chip thickness of h= 0.15 mm for all experiments, while the cutting speed was varied between v_c = 30 … 150 m/min (see Table 1). Each experiment was conducted twice to ensure statistical reliability. For measuring the maximum burr height of the experiments, the confocal microscope *Confovis DUO Vario* was used. For each experiment, three measuring areas with a size of 250 × 250 µm were recorded.

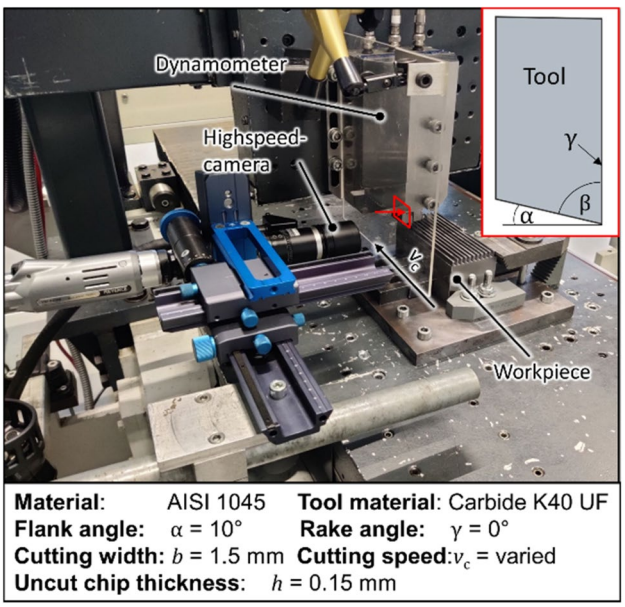

Fig. 3 Experimental setup for the cutting experiments

Table 1 Experiment overview

Experiment number	1	2	3
Cutting speed v_c	30 m/min	90 m/min	150 m/min
Uncut chip thickness h	0.15 mm	0.15 mm	0.15 mm

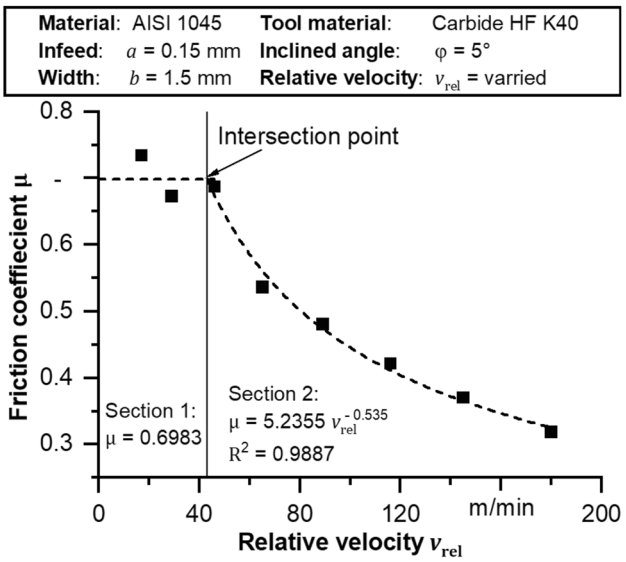

Fig. 4 Sectioned friction model as a function of relative speed

Then the maximum burr height of each area was determined, and the mean value was calculated.

5 Friction experiments

The friction model, along with the flow stress model, is the most important input parameter in a chip formation simulation. In order to be able to describe the friction behaviour realistically, characterization experiments are being conducted. The friction coefficient is the quotient of the tangential and normal forces. Taking into account the inclination angle φ, these are calculated as follows:

$$F_t = F_y \cos(\varphi) - F_x \sin(\varphi) \tag{3}$$

$$F_n = F_y \sin(\varphi) + F_x \cos(\varphi) \tag{4}$$

Hereby, F_x represents the measured force parallel and F_y normal to the relative velocity. Figure 4 shows the friction coefficient over the relative speed for the contact of AISI 1045 with a grounded cemented carbide main body. At lower speeds, up to $v_{rel} = 46$ m/min, the friction coefficient remains at a high level with a mean value of $\mu = 0.6983$. With increasing speeds, the friction coefficient is falling monotonically, reaching $\mu = 0.3188$ at $v_{rel} = 180$ m/min. This behaviour can be seen repeatedly in the literature; see [28, 29]. Saelzer et al. [27] also observed this behaviour and did a detailed analysis of the adhered material of the surface on the main body. They showed that the amount of adhered material did not change significantly below relative velocities $v_{rel} < 46$ m/min. However, as the relative speed increased, the amount of adhered material decreased, and then a bluish discoloration appeared. This implies a change in the underlying friction mechanisms, from primarily adhesion to a combination of adhesion and abrasion. This can be attributed to a multitude of different causes. On the one hand, adhesion is a time-dependent process, and the contact time between the main and counter body decreases. On the other hand, more heat is dissipated, causing a softening of the counter body. Therefore, the mechanical resistance of the abrasive friction component reduces. Additionally, oxidation, which is implied by the bluish discoloration, can reduce the friction coefficient [30].

In order to model the prevailing friction mechanisms that occur due to varying relative speeds, a sectioned definition of the friction is chosen. In section 1, a constant friction coefficient is assumed because the material adhesion behaviour did not change notably and the friction coefficient shows no tendency. For relative speeds above $v_{rel} = 46$ m/min, a power function is proposed. To ensure a continuous friction model, the intersection point of the functions from sections 1 and 2 is calculated. This equates to the following coulomb friction model:

$$\mu(v_{rel}) = \begin{cases} 0.6983, & v_{rel} < 43.19 m/min \\ 5.2355 v_{rel}^{-0.535}, & v_{rel} \geq 43.19 m/min \end{cases} \tag{5}$$

6 Cutting experiments

Following, the results of the cutting experiments are being presented. Figure 5 shows the influence of the cutting speed on the forces F_c and F_p as well as the maximum burr height h_b. Starting at a cutting speed of $v_c = 30$ m/min, the cutting force amounts to $F_c = 821$ N decreasing monotonically to $F_c = 611$ N at $v_c = 150$ m/min. This reduction can be attributed to the thermal softening of the workpiece material caused by the higher cutting power. On the contrary, the passive force remains unchanged at $F_p = 470$ N from $v_c = 30$ to 90 m/min. This is unexpected because for a rake angle of $\gamma = 0°$, the passive force is mainly caused by the friction along the secondary shear zone, and the friction experiments demonstrated a strong speed dependency. Due to this, the passive force should decrease with an increase of the cutting speed. However, the passive force reduces to $F_p = 369$ N at $v_c = 150$ m/

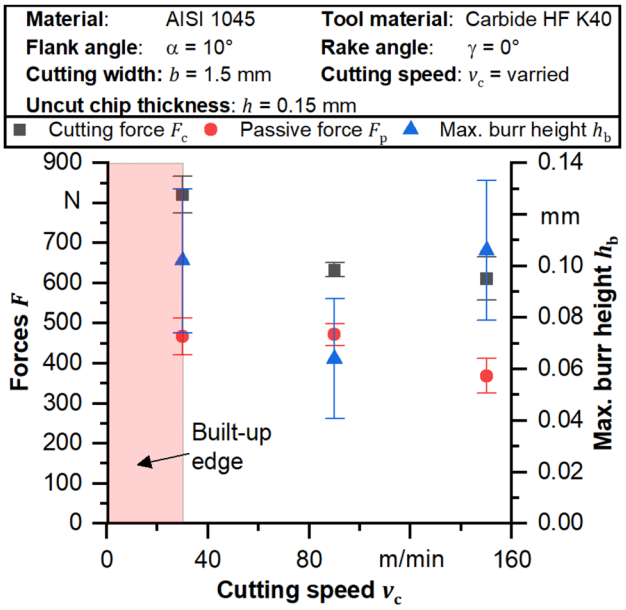

Fig. 5 Results of the cutting experiments; error bars indicate the standard deviations

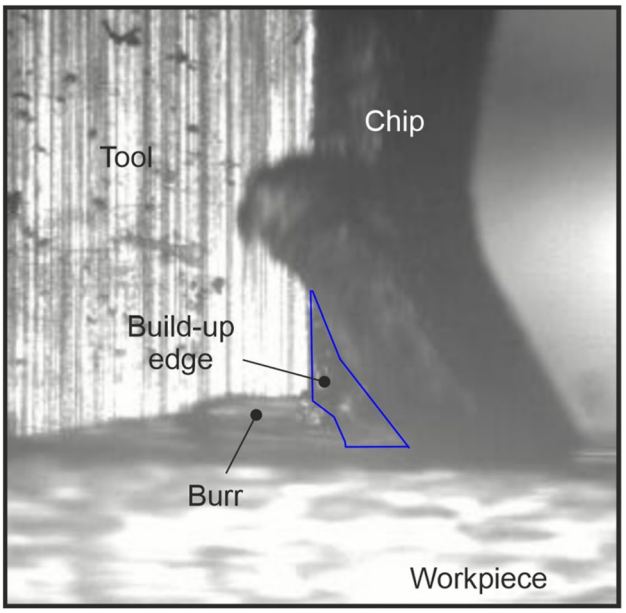

Fig. 6 High-speed recording of a built-up edge for $v_c = 30$ m/min

min, showing the anticipated behaviour. An analysis of the high-speed recordings revealed a built-up edge (BUE) at a cutting speed of $v_c = 30$ m/min (Fig. 6). This coincides with the observed adhesion behaviour of the friction experiments. Due to the BUE, the uncut chip thickness and the effective rake angle are changed uncontrollably, whereby a comparison of the forces with this cutting speed is not conclusive.

Subsequently, the comparison of the maximum burr height is conducted. It amounts to $h_b = 102$ and 64 µm for the cutting speeds $v_c = 30$ and 90 m/min, respectively. The stark difference in these values can be attributed to the BUE because it changes the uncut chip thickness, which strongly influences the maximum burr height; see [24, 25]. Increasing the cutting speed to $v_c = 150$ m/min causes an increase of the maximum burr height to $h_b = 106$ µm. However, according to the literature, e.g. [25], the burr height decreases with an increase in cutting speed. This can be attributed to a reduced shear strain during chip formation ($h_b = h_b(\varepsilon_\tau, \dots)$) [11]. A qualitative explanation can be deduced using fundamental equations of orthogonal cutting. Based on Merchant's shear plane model, the shear strain in orthogonal cutting can be derived as a function of the rake angle and shear angle ϕ (Eq. (6)). Additionally, the shear angle can be expressed depending on the rake angle and the apparent friction coefficient μ (Eqs. (7) and (8)):

$$\varepsilon_\tau = \frac{\cos\ \gamma}{\cos\ (\phi - \gamma) \sin\ \phi} \tag{6}$$

$$\phi = \frac{\pi}{4} - \frac{\rho}{2} + \frac{\gamma}{2} \tag{7}$$

$$\rho = \arctan\ \mu \tag{8}$$

In summary, it can be concluded that $h_b = h_b(\gamma, \mu, \dots)$. The friction experiments showed a strong speed dependency of the friction coefficient. This correlation means that less material is displaced laterally due to the reduced friction. However, Merchant's analysis does not consider the material properties. A higher cutting speed does have a positive correlation with the temperatures during chip formation. As a result, the workpiece material offers less resistance to deformation, leading to increased material side flow, and consequently, the burr size increases. Both effects have a contrary influence on the burr size, whereby the reduction due to less friction is expected to prevail due to its strong speed dependency at the investigated cutting speeds. A possible reason for the observed deviant behaviour is the dynamic compliance of the machine tool. Figure 7 illustrates an excerpt of the measured cutting force signal for $v_c = 150$ m/min. It is evident that the force signal has a sinusoidal deviation with an amplitude of $A \approx 100$ N around the mean value of $F_c = 611$ N, which is characteristic for a dynamic behaviour. This causes a superimposed relative motion between the tool and workpiece, causing a modulation of the uncut chip thickness. Therefore, it is assumed that the maximum burr heights coincide with

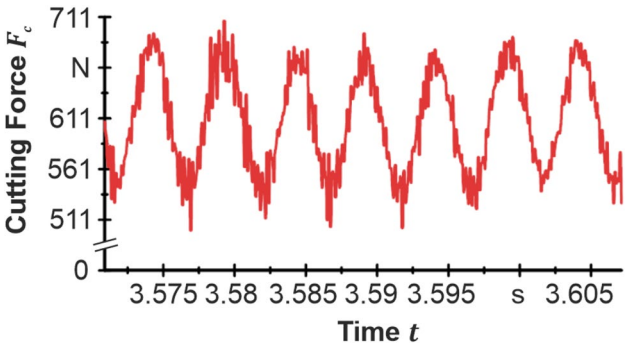

Fig. 7 Excerpt of the force signal for $v_c = 150$ m/min

the maximum peak value of the force signal. This behaviour cannot be seen in the force signals with lower cutting speeds and can be confirmed by comparing the standard deviation of the cutting forces $\sigma_c = 18$ and 54 N for $v_c = 90$ and 150 m/min, respectively (see Fig. 5).

In order to further analyse the burr formation process, a recording of the high-speed camera for an experiment with a cutting speed of $v_c = 30$ m/min is shown in Fig. 8. It illustrates the material side flow of the burr formation zone during cutting. With increasing cutting length, this material is strained, sheared and tore. Thereby, an inconsistent burr formation can be observed. The sideways displaced workpiece material fractures along the boundary of either the workpiece or chip. In the latter case, a significant burr is formed on the workpiece. The inconsistency in burr formation can be attributed to the material inhomogeneity and dynamic effects of the machine tool.

7 Chip formation simulation

In this section, a 3D FE simulation of the planing cutting process capable of predicting the maximum burr height is being developed. For this, the commercial simulation software DEFORM-3D v13.1.1 is used. Figure 9 displays an overview of the essential geometric boundary conditions and cutting parameters. The geometric boundary conditions are identical to the cutting experiments, except for the workpiece length $l_w = 15$ mm and height $h_w = 2$ mm. These dimensions have been reduced in order to reduce the model size and hence the computational time. However, it was ensured that the simulation reached a stationary state concerning the forces and maximum burr height. The tool is assumed to be a rigid body, while the workpiece is characterized by plastic deformation behaviour with isotropic hardening. The flow stress σ_f of the workpiece is calculated using the well-established Johnson–Cook model [31]. This model describes the flow stress as a function of strain ε, strain rate $\dot{\varepsilon}$ and temperature T:

$$\sigma_f = (A + B\varepsilon^n)\left(1 + C\ \ln\left(\frac{\dot{\varepsilon}}{\dot{\varepsilon}_0}\right)\right)\left(1 - T_h^m\right) \tag{9}$$

Thereby, A, B, n, C and m are material parameters, which are adopted from Jasper and Dautzenberg [32] (see Table 2). $\dot{\varepsilon}_0$ is the reference strain rate and T_h the

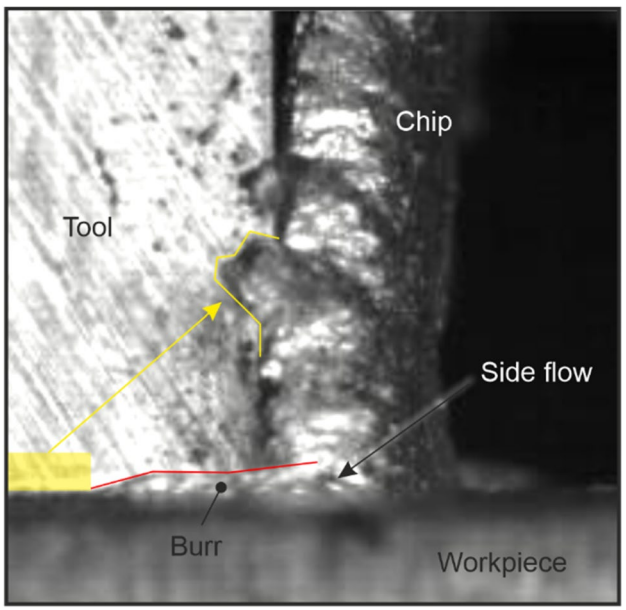

Fig. 8 Recording of the high-speed camera of the chip formation zone

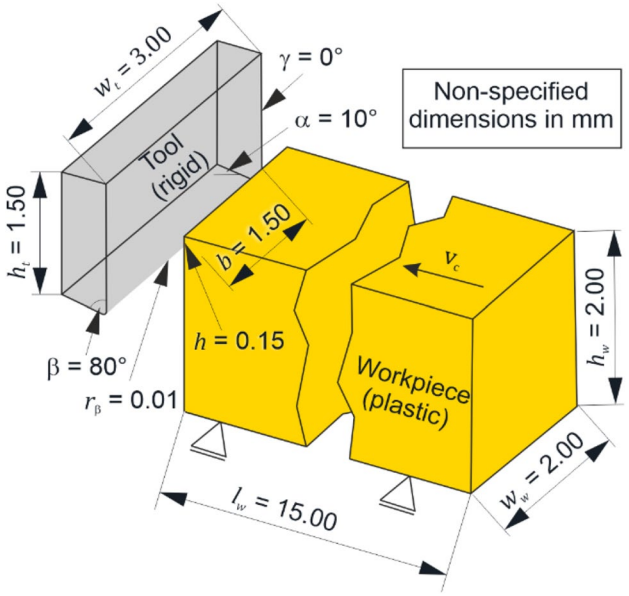

Fig. 9 Simulation setup

Table 2 Johnson–Cook flow stress model parameters for AISI 1045 [32]

Parameter	A	B	n	C	m	$\dot{\varepsilon}_0$	T_m
Value	553	601	0.234	0.0134	1	1/s	1460 °C

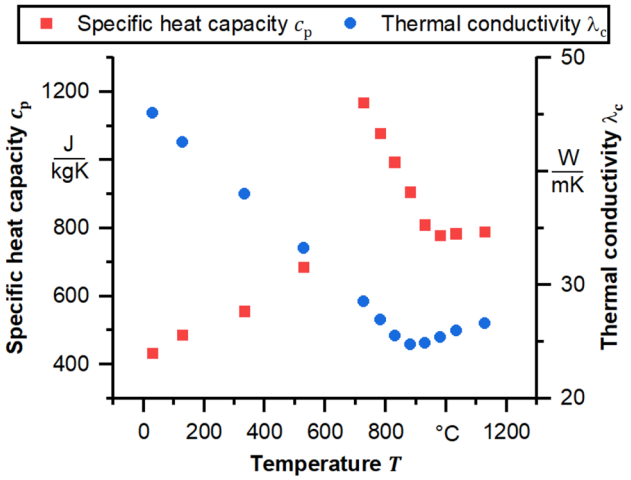

Fig. 10 Specific heat capacity and thermal conductivity depending on the temperature

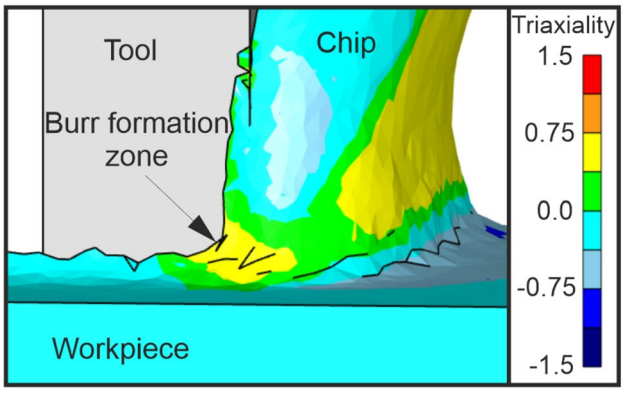

Fig. 11 Triaxiality distribution of chip formation in oblique cutting

homologous temperature. This temperature describes the relationship between the absolute temperature T and melting temperature T_m considering the reference temperature T_r:

$$T_h = \frac{T - T_r}{T_m - T_r} \tag{10}$$

For modelling, the thermal conductivity and specific heat capacity values from Grzesik and Nieslony [33] (see Fig. 10) are adopted. Their data set is chosen, because it considers the change in specific heat capacity when reaching the Curie temperature at approximate $T = 720$ °C, which can influence the thermo-mechanical load spectrum significantly.

According to Zorev [34], the contact length l_c between the chip and the tool's rake face can be divided into two distinct zones—the sticking and sliding zone. The former is characterized by high-contact normal stresses, which exceed the flow stress of the workpiece material. Therefore, the shear flow stress is reached causing shearing in the softer material, i.e., the workpiece. For this reason, there is no relative movement at the surfaces, hence the name-sticking zone. Instead, there is a sliding motion within the material. To describe the friction coefficient in this zone, the shear friction model is suitable because it is independent of the contact normal stress. In this work, a constant shear modulus of $m = 1$ is assumed. In the sliding zone, the contact normal pressure is lower, so that the shear flow stress is not reached. This results in a relative movement between the surfaces, and the coulomb friction model is valid. Thereby, a sectioned speed-dependent coulomb friction model based on the friction experiments is utilized; see Fig. 4.

Burr formation is closely linked to ductile fracture [25]. In general, the fracture locus changes depending on the loading conditions. Therefore, stress triaxiality η and the normalized lode angle $\overline{\theta}$ have been incorporated in ductile fracture formulations [35]. The former is defined as the ratio of the mean stress σ_m and the van Mises equivalent stress σ_{eq}:

$$\eta = \frac{\sigma_m}{\sigma_{\text{eq}}} \tag{11}$$

Positive values indicate a tensile stress state, whereby the enlargement and coalescence of voids is elevated. This leads to more damage in comparison to a compressive stress states, where the void growth is hindered [36, 37]. The normalized lode angle accounts for the qualitative influence of shear, tension or compression and affects the shape of the fracture locus. However, within this work, the influence of the lode angle is not considered. This simplification can be attributed to investigations by Bai [35], which have shown a decrease of the influence of the lode angle at high triaxialities for AISI 1045.

Figure 11 illustrates the triaxiality distribution of the chip formation focusing on the burr formation zone. Both the burr formation zone and the free chip surface are exposed to positive triaxialities $\eta > 0.375$. Additionally, high equivalent strains greater than $\varepsilon_{\text{eq}} > 7$ can be observed in the burr formation zone. For this reason, the Johnson–Cook ductile fracture model [38] is being implemented. This model defines

the fracture strain as a function of the triaxiality, strain rate and temperature:

$$\varepsilon_f = \left(D_1 + D_2 e^{-D_3 \eta}\right)\left(1 + D_4 \ln\left(\frac{\dot{\varepsilon}}{\dot{\varepsilon}_0}\right)\right)\left(1 - D_5 T_h\right) \quad (12)$$

Thereby, $D_1 \ldots D_5$ are material parameters, which are adopted from Rohr et al. [39] (see Table 3). The accumulated damage value is calculated as an integral over the equivalent strain ε_{eq} and failure strain ε_f as follows:

$$D = \int_0^{\varepsilon_{eq}} \frac{\varepsilon_{eq}}{\varepsilon_f} d\varepsilon_{eq} \leq D_{crit} = 1 \quad (13)$$

Once the accumulated damage value reaches the critical damage value D_{crit}, the flow stress of the element is reduced according to the softening parameter p, which is assumed to be $p = 10\%$ in this work:

$$\sigma_y^* = \sigma_y \, p \quad (14)$$

Following the definition of the input parameters for the FE simulation, a detailed analysis of the meshing strategy is conducted. The tool is discretized with 150,000 elements, whereby a mesh window around the cutting edge refines the element size locally. The workpiece mesh is defined via a minimum element size e_{min} and a size ratio of $r = 8$. Thereby, the mesh size is refined locally depending on the gradients of strain and strain rate as well as the damage. In order to select an appropriate minimum element size, a convergence analysis is conducted. Figure 12 shows the influence of the minimum element size e_{min} on the forces F and maximum burr height h_b. For the calculation of the mean value of the maximum burr height, a combined approach of the available tools of DEFORM and a python script is used. Thereby, the average value of the 15 maximum burr height values is calculated. The minimum element size is defined relative to the uncut chip thickness to ensure similarity with varying cutting parameters for further investigations. For a minimum element size of $e_{min} = h/2$, the cutting force amounts to $F_c = 688$ N. Reducing the element size to $e_{min} = h/5$ causes an increase of the cutting force to $F_c = 726$ N. A further reduction of the minimum element size shows no significant change. The passive force shows the same convergence behaviour. Starting with a value of $F_p = 195$ N at minimum element size of $e_{min} = h/2$, it is almost constant for $e_{min} < h/5$ at $F_p \approx 273$ N. Therefore, the forces converge for $e_{min} < h/5$. On the contrary, the maximum burr height shows no convergence even for a minimum

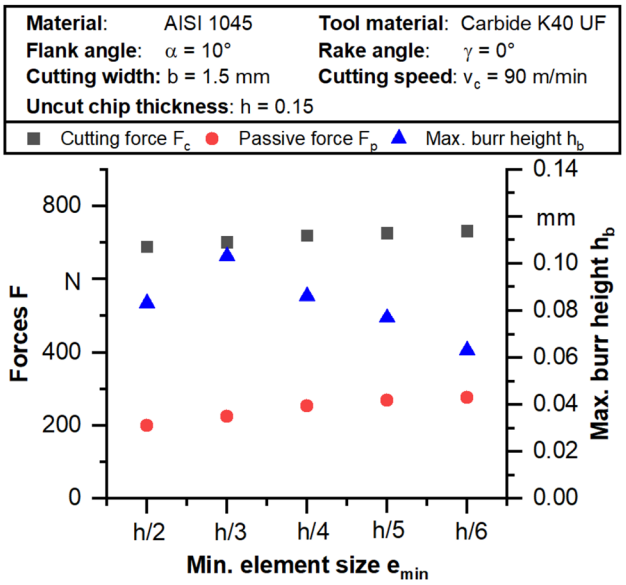

Fig. 12 Convergence analysis

element size up to $e_{min} = h/6$. For a very course mesh ($e_{min} = h/2$), the burr geometry cannot be predicted reliably; therefore, this data point is not conclusive. Refining the mesh to $e_{min} = h/3$ results in a maximum burr height of $h_b = 0.103$ mm. Further refinement leads to a monotonically decrease resulting in $h_b = 0.063$ mm for $e_{min} = h/6$. This behaviour can be attributed to the pathological mesh size dependence of local continuum damage models [40]. At the crack tip of the burr formation, the stress and strain gradients are very high. For a fine mesh, the Gauss points will be closer to the crack tip, leading to an earlier initiation of the softening [41]. This explains the reduction of the maximum burr height with a decrease in element size. For this reason, a simple adoption of the damage parameters for a damage model is not valid. To overcome the pathological mesh size dependence, nonlocal damage models are being developed, e.g. [40, 42]. However, the implementation of such a model is outside the scope of this work. Another possibility is a calibration of a damage model for a specific element size. In this case, the maximum burr height using a minimum element size of $e_{min} = h/6$ almost matches those of the experiments. For this reason, the element size $e_{min} = h/6$ is used, and no further calibration of the damage model is necessary.

Table 3 Johnson–Cook damage model parameters for AISI 1045 [38]

Parameter	D_1	D_2	D_3	D_4	D_5	$\dot{\varepsilon}_0$	T_m
Value	0.48	5	−3.7	0	0 ($T < 623$ K) and 5.5 ($T > 623$ K)	1/s	1460 °C

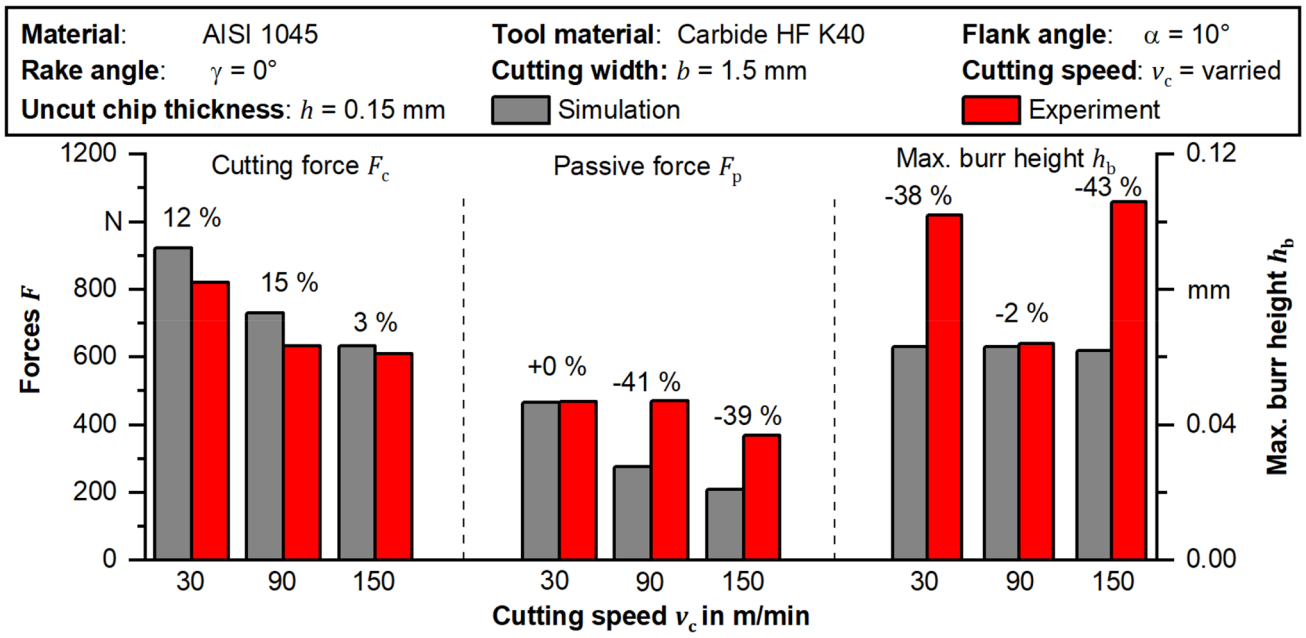

Fig. 13 Comparison of the simulative and experimental force and maximum burr height values

8 Results of the chip formation simulation

Next, the simulative and experimental results are discussed and compared; see Fig. 13. In the simulation, the cutting and passive forces are falling monotonically with an increased cutting speed. This behaviour can be attributed to the thermal softening of the workpiece, as well as a decreased friction coefficient in the secondary shear zone. Both trends are consistent with those from the experiments, except for the passive force at $v_c = 30$ m/min. This deviation is caused by the observed BUE, whereby a comparison with this data point is not conclusive. In general, the predicted cutting force, not considering $v_c = 30$ m/min, is being overestimated by an average of 9%. On the contrary, the passive forces are being strongly underestimated by an average of −40%. This behaviour can be seen repeatedly in the literature. Laakso et al. [43] studied this in detail, reasoning that the ploughing force component is underestimated in non-elastic simulations. Therefore, they investigated a model with an elastoplastic workpiece and an elastic tool with different friction models. It was concluded that the friction affects the passive force only up to 50%, which coincide with the predicted forces in this work.

The maximum burr height in the simulation evaluates to $h_b = 0.057$, 0.065 and 0.059 mm for $v_c = 30$, 90 and 150 m/min, respectively, and thus shows no tendency. This is a contradiction to the reasoning from Eqs. (6) to (8), which led to the conclusion $h_b = h_b(\gamma, \mu, \dots)$. Under the consideration of the friction experiments ($\mu = \mu(v_{rel})$), the maximum burr height should decrease with higher cutting speeds. To investigate this further, the shear angle at the distance $d = 0.25$ mm from the minor cutting edge is evaluated (Fig. 14). It evaluates to $\phi = 23$, 27 and 28° for $v_c = 30$, 90 and 150 m/min, respectively. This suggests less friction in the secondary shear zone with an increase in cutting speed. Due to this, the chip speed near to the cutting tool increases, resulting in an increase in shear angle, lower forces and an increase in chip curl. For further considerations, the burr volume per unit of length is determined. It decreases from $V_b = 3.12$ to 2.43 and to 2.19 10^{-3} mm^3/mm for $v_c = 30$, 90 and 150 m/min, respectively. This shows the expected negative correlation between the cutting speed and the burr volume, which is caused by a change in friction. A possible explanation for the deviant behaviour of the maximum burr height in the simulation is the fact that burr formation is closely linked to a non-physical remeshing algorithm. Figure 15 illustrates a 2D schematic model of this process. Due to the softening of the damage model in the burr formation zone, a few elements are being distorted heavily, triggering remeshing. Thereby, the material is distributed evenly between the chip and the workpiece. This is a fundamental difference to the burr formation in the experiments, whereby the displaced workpiece material adheres either to the chip or workpiece (Fig. 8). A comparison between experimental and simulated maximum burr heights shows a poor prediction quality for $v_c = 30$ and 150 m/min. This can be attributed to the simulation's limitation in accounting for the influence of a BUE ($v_c = 30$ m/min) or an increase in the dynamic behaviour of the machine tool ($v_c = 150$ m/min). Nevertheless, in absence of these effects, the simulation shows a good accuracy ($v_c = 90$ m/min).

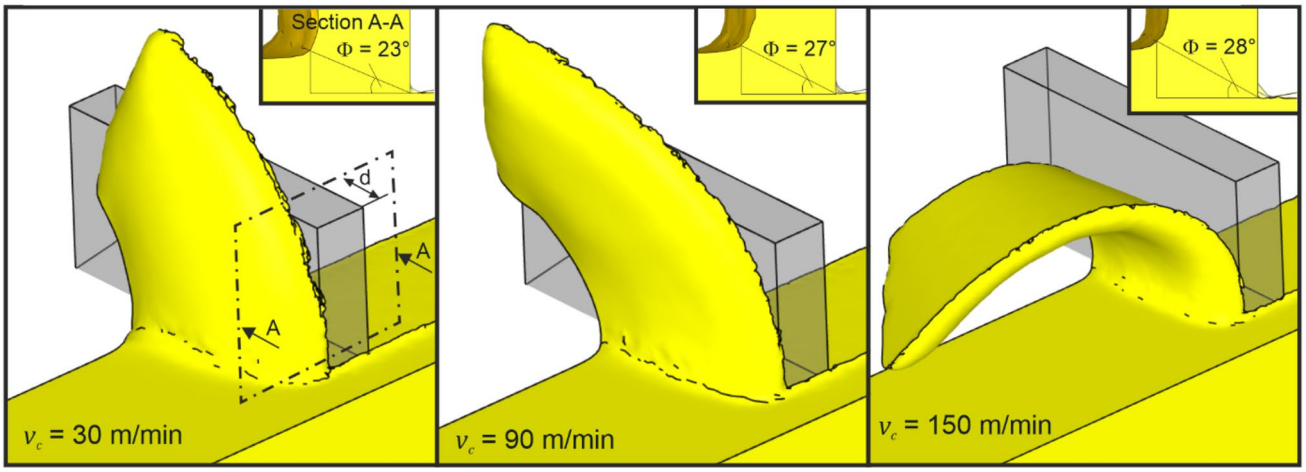

Fig. 14 Comparison of chip formation; evaluation of shear angle for $d = 0.25$ mm

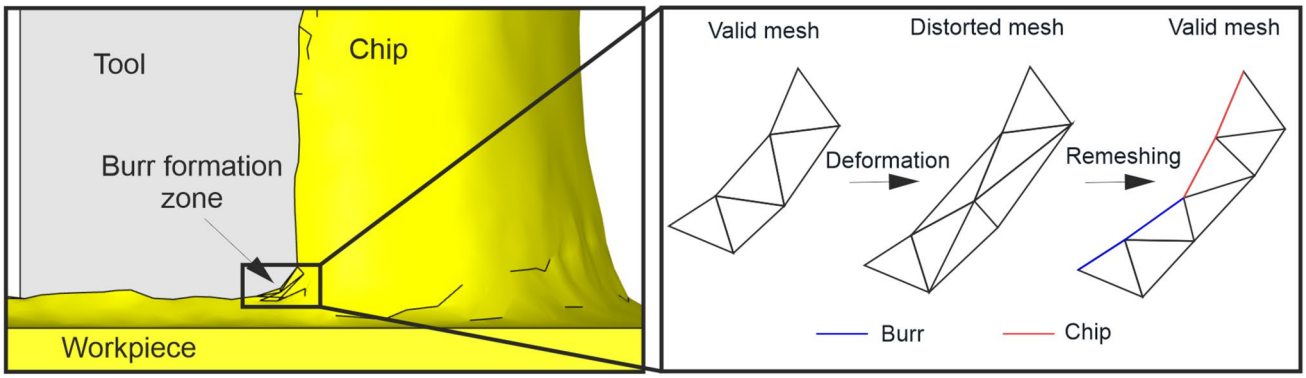

Fig. 15 3D FE simulation of chip formation (left) and 2D schematic model for burr formation due to remeshing (right)

Finally, a chip formation simulation considering elasto-plastic workpiece material for $v_c = 90$ m/min is conducted, whereby the model otherwise remains unchanged. A comparison of the simulation with non-elastic material behaviour reveals an increase in forces; see Fig. 16. This can be explained by the elastic recovery of the workpiece material and confirms the analysis of Laakso et al. [43]. Nevertheless, the prediction quality of the cutting force worsens. This can be attributed to the fact that the flow stress model was taken from the literature, whereby deviations in the microstructure of the material cannot be excluded. Lastly, comparing the maximum burr height, a slight increase can be observed, which can be attributed to the elastic deformation of the material. On the contrast, the normalized burr volume increases significantly from $V_b = 2.43$ to 4.01×10^{-3} mm^3/mm. As with the simulations with the varying cutting speed, the maximum burr height is less sensitive to changes than the normalized burr volume, which may be caused by the non-physical remeshing algorithm. Therefore, the maximum burr height might not be an appropriate characteristic for Lagrangian chip formation simulations where remeshing is necessary.

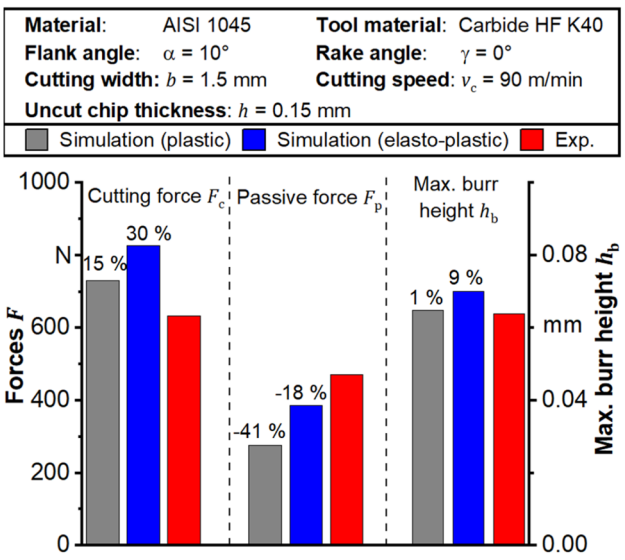

Fig. 16 Comparison of simulations with plastic and elastoplastic workpiece behaviour with the cutting experiment

9 Conclusion and outlook

The goal of this work was to develop a 3D FE simulation capable of predicting the maximum burr height for planing because the dimensions of the burrs can have the same magnitude as the structure itself. For this reason, novel fluid mechanical investigations of non-idealized sawtooth structures were conducted, demonstrating a sensitive performance concerning the resulting normalized mass flow rate depending on the tip geometry. In order to ensure an accurate description between the workpiece and tool in the simulation, friction experiments were performed. Thereby, a hybrid friction model with a speed-dependent coulomb friction model was utilized. Additionally, planing experiments were carried out in order to generate validation data for the simulation and improve the process comprehension. Next, a 3D FE simulation, including a triaxiality-dependent damage model, was established. This damage model was chosen because of a new observation of high positive triaxialities $\eta > 0.375$ in the burr formation zone. For this model, a convergence study was conducted. Thereby, the pathological mesh size dependence of continuum damage models was observed. Due to this, a calibration of the damage model was performed. Furthermore, a comparison of the experimental and simulative results was carried out, showing a reasonable agreement (+ 15%) of the cutting force. In contrast, the passive force was greatly underestimated (− 41%), which could be attributed to the underestimated ploughing force component in non-elastic chip formation simulations. Moreover, the maximum burr height for $v_c = 90$ m/min was predicted with good accuracy (− 2%). However, the prediction of the simulation for the other cutting speeds regarding the maximum burr height was poor due to the observed BUE (v_c= 30 m/min) and dynamic behaviour of the machine tool (v_c= 150 m/min) in the experiments. Additionally, it was observed that the normalized burr volume is more sensitive to a change in the simulation than the maximum burr height, because the latter is significantly influenced by a non-physical remeshing algorithm, which was described in a schematic model. This implies that the maximum burr height might not be an appropriate characteristic for Lagrangian chip formation simulations where remeshing is necessary. To the authors' best knowledge, this was not discussed in prior publications.

This hypothesis will be investigated in more detail in future research using an Abaqus-coupled Eulerian–Lagrangian model, which does not require remeshing. Additionally, cutting experiments with an acceleration sensor will be conducted, whereby different values for the cutting speed, rake angle and uncut chip thickness are considered. This information will be used to implement the dynamic machine tool behaviour in the simulation and improve the prediction quality of the simulation.

Funding Open Access funding enabled and organized by Projekt DEAL. Funded by the Deutsche Forschungsgemeinschaft (DFG, German Research Foundation). Gefördert durch die Deutsche Forschungsgemeinschaft (DFG) – Projektnummer 513663608.

Declarations

Competing interests The authors declare no competing interests.

References

1. Jousten K (Ed.) (2018) Handbuch Vakuumtechnik, 12., neu bearbeitete Auflage ed. Springer Vieweg, Wiesbaden, Heidelberg, 1129 pp
2. Sazhin O (2020) Rarefied gas flow through a rough channel into a vacuum. Microfluid Nanofluid 24(4). https://doi.org/10.1007/s10404-020-2330-y
3. Müller R (2013) Spaltströmung mit Wärmeübertragung in Vakuumpumpen. Dissertation, Kaiserslautern, 191 pp
4. Denkena B, Kästner J, Wang B (2010) Advanced microstructures and its production through cutting and grinding. CIRP Ann 59(1):67–72
5. Câmara MA, Rubio JC, Abrão AM, Davim JP (2012) State of the art on micromilling of materials, a Review. J Mater Sci Technol 28(8):673–685
6. Joao D, Milliken N, Bordatchev EV, Tutunea-Fatan OR (2019) Axial strategy for ultraprecise single point cutting of V-grooves Case 1: constant chip thickness. Procedia Manuf 34:440–445
7. Bird GA (1994) Molecular gas dynamics and the direct simulation of gas flows. Clarendon Press, Oxford
8. Pleskun H, Brümmer A (2022) Gas–surface interactions of a Couette–Poiseuille flow in a rectangular channel. Phys Fluids 34(8). https://doi.org/10.1063/5.0099256
9. Klocke F (2018) Fertigungsverfahren 1. Springer Berlin Heidelberg, Berlin, Heidelberg, 683 pp
10. Gillespie LK, Blotter PT (1976) The formation and properties of machining burrs. J Eng Ind 98(1):66–74
11. Nakayama K, Arai M (1987) Burr formation in metal cutting. CIRP Ann 36(1):33–36
12. Beier H-M, Nothnagel R (2015) Praxisbuch Entgrattechnik: Wegweiser zur Gratminimierung und Gratbeseitigung für Konstruktion und Fertigung, 2, überarbeitete und erweiterte, Auflage. Hanser, München, p 202
13. Pekelharing AJ (1980) Cutting tool damage in interrupted cutting. Wear 62(1):37–48

14. Sung-Lim K, Dornfeld DA (1996) Analysis of fracture in burr formation at the exit stage of metal cutting. J Mater Process Technol 58(2–3):189–200
15. Chern G-L, Dornfeld DA (1996) Burr/breakout model development and experimental verificatioN. J Eng Mater Technol 118(2):201–206
16. Chern G-L (2006) Study on mechanisms of burr formation and edge breakout near the exit of orthogonal cutting. J Mater Process Technol 176(1–3):152–157
17. Zannoun H, Schoop J (2023) Analysis of burr formation in finish machining of nickel-based superalloy with worn tools using micro-scale in-situ techniques. Int J Mach Tools Manuf 189:104030
18. Min S, Dornfeld DA, Kim J, Shyu B (2001) Finite element modeling of burr formation in metal cutting. Mach Sci Technol 5(3):307–322
19. Asad M, Ijaz H, Khan MAA, Asgharyaseen A, Waqar T, Aziz Afzal A (2020) A numerical insight on machining burr formation: a comprehension to optimization approach. Mater Today: Proc 33:1792–1799
20. Zou Z, Liu L, Li B, Deng W (2016) Research on burr formation mechanism in metal cutting with a backup material. Int J Adv Manuf Technol 86(5–8):1895–1907
21. Hashimura M, Ueda K, Dornfeld D, Manabe K (1995) Analysis of three-dimensional burr formation in oblique cutting. CIRP Ann 44(1):27–30
22. Ko S-L, Dornfeld DA (1996) Burr formation and fracture in oblique cutting. J Mater Process Technol 62(1–3):24–36
23. Li P, Wang C, Zeng L, Liu H, Wang Y (2023) Analytical modeling of Poisson burr formation in the machining of Al6061 with interface constraint. Int J Adv Manuf Technol 129(1–2):353–374
24. Deng WJ, Xie ZC, Lin P, Xu TK (2012) Study on burr formation at the top edge in rectangular groove cutting. Adv Mater Sci Eng 2012:1–9
25. Pang X, Liu X, Zhang J, Deng W (2021) Investigation on the modelling and characterization of top edge burr formation in slotting finned tube. Int J Adv Manuf Technol 112(1–2):537–551
26. Puls H, Klocke F, Lung D (2014) Experimental investigation on friction under metal cutting conditions. Wear 310(1–2):63–71
27. Saelzer J, Berger S, Iovkov I, Zabel A, Biermann D (2021) Modelling of the friction in the chip formation zone depending on the rake face topography. Wear 477:203802
28. Rech J, Arrazola PJ, Claudin C, Courbon C, Pusavec F, Kopac J (2013) Characterisation of friction and heat partition coefficients at the tool-work material interface in cutting. CIRP Ann 62(1):79–82
29. Smolenicki D, Boos J, Kuster F, Roelofs H, Wyen CF (2014) In-process measurement of friction coefficient in orthogonal cutting. CIRP Ann 63(1):97–100
30. Neugebauer R, Bouzakis K-D, Denkena B, Klocke F, Sterzing A, Tekkaya AE, Wertheim R (2011) Velocity effects in metal forming and machining processes. CIRP Ann 60(2):627–650
31. Johnson GR, Cook WH (1983) A constitutive model and data for metals subjected to large strains, high strain rates and high temperatures. Proceedings of the 7th International Symposium on Ballistics 541–547
32. Jaspers S, Dautzenberg J (2002) Material behaviour in conditions similar to metal cutting: flow stress in the primary shear zone. J Mater Process Technol 122(2–3):322–330
33. Grzesik W, Nieslony P (2004) Prediction of friction and heat flow in machining incorporating thermophysical properties of the coating–chip interface. Wear 256(1–2):108–117
34. Zorev N (1963) Inter-relationship between shear processes occurring along tool face and shear plane in metal cutting. Proceedings of the International Research in Production Engineering Conference (ASME) 42–49
35. Bai Y (2008) Effect of loading history on necking and fracture. PhD thesis, Massachusetts, 262 pp
36. McClintock FA (1968) A criterion for ductile fracture by the growth of holes. J Appl Mech 35(2):363–371
37. Rice JR, Tracey DM (1969) On the ductile enlargement of voids in triaxial stress fields∗. J Mech Phys Solids 17(3):201–217
38. Johnson GR, Cook WH (1985) Fracture characteristics of three metals subjected to various strains, strain rates, temperatures and pressures. Eng Fract Mech 21(1):31–48
39. Rohr I, Nahme H, Thoma K (2004) Charakterisierung des Schädigungsverhaltens von duktilem Stahl, Werkstoffprüfung 2004. Tagungsband : Konstruktion, Qualitätssicherung und Schadensanalyse; 25. - 26. November 2004 in Neu-Ulm, 2004.
40. Larsson R, Razanica S, Josefson BL (2016) Mesh objective continuum damage models for ductile fracture. Numer Meth Eng 106(10):840–860
41. Besson J (2010) Continuum models of ductile fracture: a review. Int J Damage Mech 19(1):3–52
42. Sprave L, Schowtjak A, Meya R, Clausmeyer T, Tekkaya AE, Menzel A (2020) On mesh dependencies in finite-element-based damage prediction: application to sheet metal bending. Prod Eng Res Devel 14(1):123–134
43. Laakso SV, Agmell M, Ståhl J-E (2018) The mystery of missing feed force — the effect of friction models, flank wear and ploughing on feed force in metal cutting simulations. J Manuf Process 33:268–277